Gas-assisted laser cutting of medium-section metals using spherically aberrated beams

Vladimir I. Yurevich
Viacheslav A. Grimm
Igor V. Polyakov
Andrey A. Afonyushkin
Sergey G. Gorny

Gas-assisted laser cutting of medium-section metals using spherically aberrated beams

Vladimir I. Yurevich,[a,b,][*] Viacheslav A. Grimm,[c] Igor V. Polyakov,[a] Andrey A. Afonyushkin,[a,b] and Sergey G. Gorny[a]

[a]Laser Center Ltd., 25 Piskarevsky Avenue, Saint Petersburg 195176, Russian
[b]Saint Petersburg National University of Information Technologies, Mechanics and Optics, Department of Photonics and Optical Information Technology, 49 Kronverkskiy Public Relation, Saint Petersburg 197101, Russian
[c]Saint Petersburg National University of Information Technologies, Mechanics and Optics, Department of Laser Technologies and Biomedical Optics, 49 Kronverkskiy Public Relation, Saint Petersburg 197101, Russian

Abstract. We analyzed the effects of the focal point aberrational offset in optical transport systems for high-power lasers. Transverse and near-axial laser intensity distribution transformations in the presence of both positive and negative spherical aberrations were numerically calculated and experimentally demonstrated for different strengths. We show that spherical aberration yields considerable asymmetry of the focused beam's caustic. Several optical transport systems with identical optical parameters (excluding the noncorrected axial beam spherical aberration) were designed. We examined the effects of the laser intensity profiles produced by these systems on the quality of oxygen-assisted laser cutting of medium-section mild steel. We show that high-quality cuts can be obtained for different shapes of laser intensity distribution. However, the greater the refocusing magnitude introduced by the spherical aberration correction, the more precisely the focal point position must be maintained during the laser cutting process. © *The Authors. Published by SPIE under a Creative Commons Attribution 3.0 Unported License. Distribution or reproduction of this work in whole or in part requires full attribution of the original publication, including its DOI.* [DOI: 10.1117/1.OE.54.4.044103]

1 Introduction

Laser cutting of metals and alloys is one of the most commercially valuable laser technology processes. Originating from basic research on laser–matter interaction,[1] the field has significantly developed, now offering a large arsenal of state-of-the-art techniques.[2–5] Omitting the energy and resource efficiency issues,[6] the performance of laser cutting can be captured by only two output parameters. These are the cutting speed and kerf quality. Thus, laser cutting optimization reduces to achieving the maximal cutting speed with the best kerf quality. As far as the material separation is concerned,[7] the speed can be dramatically increased. On the other hand, the cutting quality depends on many parameters. The most important and frequently discussed are the kerf geometry (accuracy, width, and taper), the surface quality (cut–edge roughness, striations morphology, and dross and burr inclusions), and the mechanical and metallurgical properties (hardness and strength, heat-affected zone, and oxide layer).[8] The number of parameters dramatically affecting the cutting quality ranges from 25[9] to 75.[4,5] These are nearly evenly divided between the workpiece properties, assist gas parameters, laser machine, and laser beam characteristics. Input–output parameters relationships are mostly nonlinear and exhibit strong interdependence. In this regard, maximal precision is provided by the studies that focus on only one input—output parameter pair. Yet, this "one parameter at one time" approach does not provide complete information on the process as a whole.

Relatively little is known regarding the aberrational distortion of laser beams due to the specifics of design and operation of transport systems of high-power laser cutters. This knowledge gap becomes critical when considering the dependence of industrial cutting quality on a particular laser intensity distribution (LID) formed by an optical system of the cutter in the laser—matter interaction region. The significance of focal point position (FPP) distance and possible range of its variation during gas-assisted laser cutting remain poorly understood. This motivated us to perform systematic studies of LID transformation in caustics with spherical aberration (SA). The obtained data were used for designing an array of optical transport systems with identical optical parameters, excluding the noncorrected axial beam SA. These systems, yielding considerably different LIDs, were placed in the same laser cutter. The root-mean-square magnitude of an unbalanced spherical wave aberration (WA_{rms}) was used as the input parameter. Dross height was chosen as the output parameter. It exhibits solidified residual melt which remains attached to the kerf–edge bottom. Together with the kerf roughness, the dross comprises a serious fault, demanding considerable postlaser treatment of the processed tools.

This paper is organized as follows. In Sec. 2, we briefly review the state of the field and the problem. Section 3 presents the study framework. Simulations of near-caustic LID shapes in the presence of SAs of various strengths and signs are reported for several fiber sources typically used in laser cutting machines. The basic findings are discussed. In Sec. 4, we describe the experimental results. First, we describe the experimental setup and methodology. Next, we characterize the beams tailored using SA. Finally,

*Address all correspondence to: Vladimir I. Yurevich, E-mail: optic@newlaser.ru

we discuss trial cuts made using these beams. Summary and conclusions are presented in Sec. 5.

2 Optical Considerations of Laser Cutting

2.1 Speed-Power-Pressure Concept

A literature review suggests that the main factors affecting a laser cutting quality are the cutting speed, the laser power, and the assist gas pressure. Radovanovic and Madic[10] reported that different combinations of these parameters have been considered in up to 67% of the cited papers. Studies addressing the joint impact of five input parameters comprised only 6%. Some studies addressed optimization by considering different combinations of input parameters. Hashemzadeh et al.[11] introduced specific point energy, SPE = Power × Beam Size/Speed and (Speed/Power)^2. Orishich et al.[12] used Peclet number, Pe = Speed × Kerf Width/Heat Diffusivity and density of the absorbed laser energy averaged over the kerf volume. The working hypothesis of the final kerf relief formation is solidification of the unstable melt flow.[13,14] Detailed investigations by Hirano and Fabbro[15,16] show that this instability is a sum of thermodynamic instability (related to the localized melting) and hydrodynamic instability (caused by the imbalance of assist gas flux and surface tension forces). The instability pattern varies along the melt flow, causing the complicated final relief of the kerf surface. Considerable physical complexity justifies the existence of the literature dedicated to empirical investigations of quality parameters. Techniques such as analysis of variances,[17–20] response surface method,[20–23] multiple regression analysis,[9,24,25] artificial neural networks,[9,26–28] and genetic algorithms[22] have been used in these studies. Results are captured as polynomials that relate a single output parameter to a set of input parameters. The studies using the cutting speed, laser power, and assist gas pressure as input parameters comprising, respectively, 100%, 77%, and 62%. Kerf surface roughness was considered as the output parameter in 70% of the studies. Kerf taper and width were considered in 46% of the studies. Yet, the obtained polynomials had different functional forms. Thus, Zaied et al.[19] reported results using a single quadratic term, but others obtained polynomials that included from 5–10[9,21,24,28] to 15[20,22,23] terms. Discordant polynomial forms are particularly appealing in light of the dramatic effect of unaccounted factors such as the environment,[24] workpiece parameters,[29] and laser beam characteristics.

2.2 Laser Beam Shape, Position, and Distortion: Causes, Effects, and Definitions

The most explored area of laser beam characteristics impact relates to the energy balance studies utilizing "cutting speed–cut front inclination angle–absorption of polarized light–thermal dynamics versus quantity of absorbed energy–quality parameters" models. Summarizing the simulations,[15,30] experiments,[13,16] and articles combining experiments and theory,[31,32] the best speed–quality relationship is achieved when the melt front inclination angle provides absorbed energy supporting maximally uniform melt flow in all melt pool regions, with minimal melt accumulation. The relationship between the averaged melt front inclination angle, kerf geometry, and laser beam size governs the averaged fraction of the beam power involved in the cutting process.[12,13]

De facto, the melt pool surface is a complex three-dimensional wavy humped structure with strongly varying local characteristics.

Existing studies[7–11,14–29] do not consider the spatial characteristics of laser beams. Nevertheless, these are accounted for by the FPP, which is one of the key factors of the cutting process. The FPP denotes the beam waist location relative to the workpiece's front surface. Accordingly, previous studies were performed with FPPs that yielded the best laser cutting performance. The details of this approach are described by Orishich et al.[12] Only in one study was the FPP used as the input optimization parameter.[28] It is obvious that the beam waist should always be located on the thin-section workpiece's surface (FPP = 0) during cold ablation cutting at extremely high intensities produced by sharp beam focusing.[33] In gas-assisted laser cutting of medium- and thick-section metals, the beam waist rarely coincides with any of the material surfaces of the cutting sheet or melt pool. In these cases, determining the optical components yielding the minimal waist size of the focused beam[34] is tangential. Wandera[35,36] showed that in the case of high beam quality fiber lasers, the FPP scales with the sheet thickness, consistent with gas and fluid dynamical aspects of melt removal from the wider kerf (see also Ref. 37). At the same time, for any fixed FPP value, an excellent cut, good cut, dross, and no cut occur with nearly equal frequency. In the case of disk lasers[35,36] characterized by considerably worse beam quality, no "cutting quality–thickness–FPP" correlation exists. Inconsistent results have been obtained for cutting aluminum alloys.[38] FPP variation affects the Gaussian beam size in the interaction region without affecting the transverse LID.[39] In real applications, the LID shape strongly varies along the propagation axis because the laser beam and the optical system are not ideal. Hence, the best FPP search amounts to finding the beam characteristics that provide an optimal (not maximal) load of the laser power into the laser—matter interaction region.[40]

The effect of the LID shape on the performance of laser technology processes has been repeatedly confirmed in experiments. Some papers directly attributed the cutting quality to fiber[2–5,18,35] and conventional[41,42] laser beam quality. Conversely, many studies reported considerable performance improvement by using non-Gaussian beams. Thus, considerably increased cutting speed is predicted when using coma-like beams.[43] A 20% increase in maximal dross-free cutting speed was experimentally demonstrated using bifocal optics.[44] Enhanced welding speed and quality were obtained using columnar and elliptical spots[45,46] and with multispot processing.[47–49] Different detectable keyhole shapes were observed for Gaussian and tophat beams.[50,51] Applications of doughnut and annular beams yielded a 20% increase in stainless steel cutting speed and higher quality holes drilled in titanium foils.[52] Common to all these studies is the absence of the beam characteristics choice concept as well as the lack of information on its actual shape for defocusing range used in every actual process.

It is well known[53,54] that aberrations in optical systems powerfully affect caustic shape distortion. In actual laser cutters, SAs of considerable strength are likely present when other primary aberrations are negligibly small. So-called design and manufacturing SAs are usually retained in laser cutter transport systems during optical design and

manufacturing. Furthermore, thermally induced distortions in high-average power laser optical systems[55,56] in typical cases of circular beams and optics are mostly characterized by spherical components.[57] Scarce research on aberrational distortions in laser beams[58,59] is likely owing to the apparent triviality of the problem. In addition, the beam quality factor[60] is widely used as a universal parameter. Thus, some studies address M^2 degradation[61,62] instead of the beam shape transformation. The M^2 value in question of the beam propagation reasonably describes near-Gaussian beams.[51,63,64] In this case, the beam size is adequately determined using second-order intensity moments.[65] Determination of 4σ — size of noticeably non-Gaussian beams becomes too time consuming. Express techniques[66,67] are not regularly applied. Introducing M^2 into the Gaussian beam equations suggests the caustic symmetry[37,62,64] that is never asserted for an aberrated beam. Furthermore, different beams may be characterized by the same M^2.[68] These facts generated a certain scepticism as to the versatility of the M^2 approach, expressed even by the author of this concept in his subsequent papers.[69] Qualitatively, it is evident that any M^2 degradation[60] as well as the dramatically rarely used Strehl ratio,[70,71] the overlapping integral,[71] and the V-parameter[66] witness some LID distortion. However, knowing the actual LID shape in an interaction region is desired. None of the above parameters, including the aberration strength in the units of Seidel and Zernike[57,72] factors, provide this knowledge.

It is clear that an LID shape distorted by aberration critically determines the laser cutting performance. An initially high beam quality and diffraction-limited optics do not satisfactorily determine the cutting quality. At the same time, the concept of speed-power-pressure implies neither no requirements on the transport system nor knowing the actual beam shape.

3 Spherical Aberration and Laser Intensity Distribution Near the Beam Waist

3.1 Paraxial Focus, the Best Focal Spot, and Focal Point Position in Aberrated Systems

The analytical description of an aberrated beam spatial shape distortion was provided by Born and Wolf in Sec. 9.4 of their monograph.[54] The aberration is most evident as a deviation of the best focus spot (BFS) from the paraxial focus plane (PFP). Assuming this deviation is constant, it does not affect laser cutting. Critically, the axial and transverse LID in the aberrated caustic dramatically differ from those obtained in the aberration-free case. The aberrations' effect can be demonstrated simply by alluding to the ray model of geometrical optics.[53] The rays normal to the surface of the distorted wavefront traveling from the exit pupil of an optical system intersect in the image space. The intersection density (i.e., intensity) depends on the wavefront distortion strength and is a function of both the axial and transverse coordinates. Consequently, cross sections at different points along the beam propagation direction are characterized by different transverse LID shapes. We define the BSF as the region with the maximal intensity and refer to "the spot" instead of "the point" because a region of indistinguishably equal intensity is always of finite size. Alternative methods of a BFS definition involve the averaging of the beam energetic characteristics. The size and position of a BFS defined in

different ways may not be consistent but the difference is small compared to the actually used FPP ranges. An optical configuration of the refractive laser cutter heads is typically telecentric[73] and the image space is limited by the nozzle size. In principle, field aberrations do not relate to the cutting head optical performance parameters. Refocusing is easily performed to add defocus for achieving the required correction of the SA for maximizing the system's point-spread function. Coma and astigmatism are close to zero in the vicinity of axial ray propagation, even in cases of certain lens misalignment.[53,54,74,75] The number of refractive surfaces of a typical transport system is sufficient for producing a diffraction-limited beam for apertures up to 0.20, assuming that the optical path is computed as a whole.[74,76] The basic problem here is that the collimating unit and the processing head are usually purchased separately, often from different vendors. Assuming that the collimating unit produces a diffraction-limited beam, a WA_{rms} of ~0.05λ is introduced using an optimized focusing singlet with an output NA of 0.06. For an optimized focusing doublet, the same WA_{rms} is achieved at an output NA of approximately 0.20.[74] Accumulation of optical components in a transport system is prevented by nonthreshold thermal phenomena related to the laser radiation absorption in the bulk and on the surfaces. The simplest and most investigated phenomenon is the laser-induced focal shift,[64,77,78] which is directly proportional to the laser fluence. Among the optical component parameters, the most significant are the absorption factor and temperature-induced index variation, $\partial n/\partial T$.[56,77,79] There is also the more delicate aspect of thermal lensing: although a thermal lens has relatively small optical power, it is strongly aberrated.[55–57,72] Chow et al.[72] estimated the wavefront distortion as a few hundredths of the wavelength per kilowatt per 1 cm length for state-of-the-art fused silica plano–plano windows. The same measurements for a commercial four-lens transport system[57] yield a wavefront error up to several wavelengths per kilowatt per total thickness of anti-reflection coated glass. Thermal phenomena significantly constrain the choice of glass, its sum length, and the number of refractive surfaces.[77,80] This tradeoff between the optical and thermal performance of a system often does not allow for a complete correction of aberration, even during preliminary optical design. Contamination of optical surfaces crucially contributes to laser-induced beam deterioration.[80] All contaminations, including the invisible ones, are a powerful source of laser heat dissipation. In this case, the speed-power-pressure-FPP correlation is lost and process failure occurs. Contaminations of reflective surfaces yield considerably smaller beam deterioration[72] because $\partial n/\partial T$ is irrelevant to thermal lensing.

Different scenarios of BFS and PFP relative locations and FPP range are schematically shown in Fig. 1. For an ideal beam propagating through an ideal optical system, the BFS_0 and PFP are colocalized at the axial origin, the transverse LID shape does not depend on the axial coordinate, and the beam is congruent over the entire propagation length.[39] The waist size $2\omega_0$ defines the Rayleigh range z_R. With spherical aberration, the BFS_p, BFS_N move in the direction opposite to the sign of wave aberration. This is also the direction in which the beam congruence is lost. We denote this region as the aberration location range (ALR). Loss of congruence causes the formation of an LID with complicated
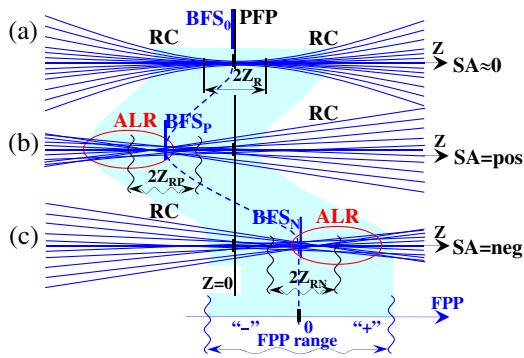
Fig. 1 Best focal spot (BFS) and paraxial focus plane (PFP) locations for: (a) the ideal beam, (b) a beam with positive, and (c) negative wave spherical aberrations (SAs). RC is the ray congruence region, aberration location range (ALR) is the aberration location range, z_R is the Rayleigh range. Blue highlighted area denotes the possible range of focal point position (FPP) used in gas-assisted laser cutting of medium-section metals.

axial and transverse patterns. Outside the ALR, the beam remains congruent. Nonetheless, both inside and outside the ALR, the Gaussian transverse shape as well as the hyperbolic envelope are frustrated proportionally to the aberration strength. The transverse LID shape associated with the SA has rotational symmetry. Inside the ALR, an initially diffraction-limited beam transforms into a sharp-edged modulated pattern. Outside the ALR, it assumes a smooth wide-winged shape with a sharp maximum. The Rayleigh range of an aberrated beam z_{RP}, z_{RN} has no strict physical definition and is introduced here only as a measure of beam size variation. The FPPs for laser cutting of medium-section metals are typically in the millimeter range.[35–38] Depending on the waist size it can exceed z_R by an order of magnitude. The

FPP = 0 case always implies that the BFS is placed on the upper surface of the sheet, as shown by the dashed line in Fig. 1. The FPP sign is determined by the coordinate choice. In our interpretation, the beam propagation direction was taken along the z axis with the zero FPP coordinate placed on the beam waist. In this way, the FPP was taken as positive when the beam waist was placed above the upper surface of the sheet. This means of framing the axes agrees with the signs' convention used in optics and consolidates the signs of all z, z_o, and FPP axes for all of the figures in the present paper. However, it is inversely related to the framing with the zero FPP placed on the front surface of the sheet.[35–38]

3.2 Numerical Simulation of the Beam Caustic in the Presence of Spherical Aberration

Simulations of beam caustics with SAs were performed using standard optical design software. An integrated finite optical system was used as the model. It was allowed to inversely alter the sign and magnitude of the aberration by changing the position of one component, resulting in relatively small variations in the system parameters. This allowed analyzing the LID shapes in caustics with similar parameters in different configurations providing wave SAs with WA_{rms} +0.004, +0.08, ±0.55, ±0.85 wavelengths ($\lambda = 1070$ nm) in BFS. The first configuration was used as the diffraction-limited sample. The BFS position for each optical configuration was determined by inducing small axial movements of the detector plane along the optical axis and searching for the maximal intensity. The simulated maximal intensity near-axial behavior plots are shown in Fig. 2. The colors and types of the curves are consistent across Figs. 2 and 3. The curves in each plot are normalized
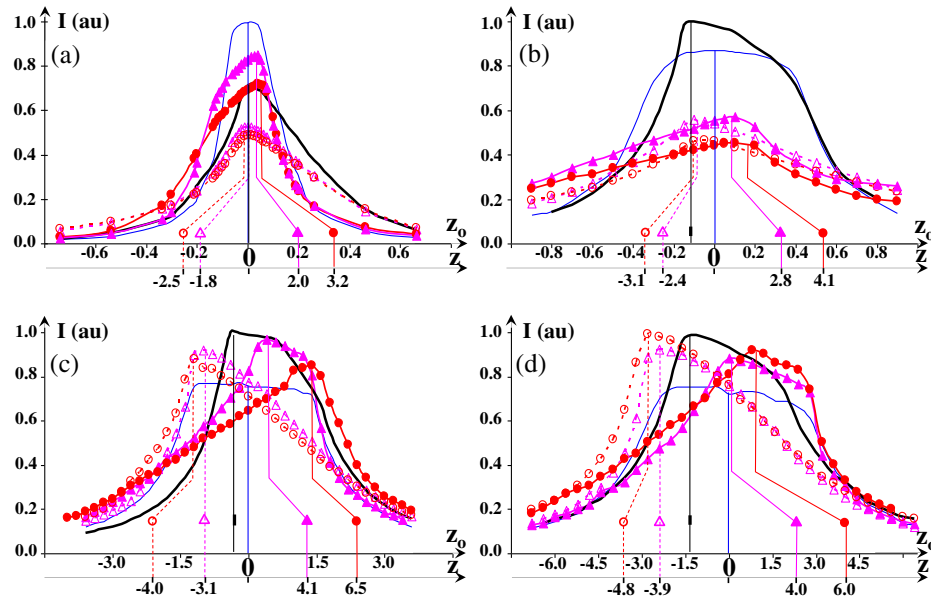

Fig. 2 Computed maximal intensity plots for the simulated systems in the presence of SAs versus the source size $2\omega_S$. (a) Gaussian source $2\omega_S = 7$ μm. Uniform sources: (b) $2\omega_S = 50$ μm, (c) $2\omega_S = 200$ μm, (d) $2\omega_S = 400$ μm. Object space NA is 0.10 and linear magnification is −1.175 for all figures. The blue thin curves refer to nearly zero SA, the black solid curves—to positive wave SA with 0.08λ WA_{rms}, the purple solid and blank triangles—to negative and positive wave SAs with 0.55λ WA_{rms}, the red solid and blank circles—to negative and positive wave SAs with 0.8λ WA_{rms}. BFS positions for the case of the two lowest SAs are placed onto z_0 axis. For larger SAs, they can be found on z axis. The curves in each plot are normalized by the absolute maximal intensity obtained using the given source.

by the absolute maximal intensity obtained using the given source. Moving the component to positions providing maximal positive and negative aberrations caused a $\pm 1.50\%$ focal length variation. The back focal distance variation was as large as $\pm 2.5\%$. Meanwhile, the maximal BFS variations were much larger owing to considerable defocus, and mostly depended on the source size. In this regard, and for clarity, we folded the curves onto each other and introduced the second longitudinal axis z_0 for the coordinate inside a given caustic. The axis z represents the absolute coordinate of the aberrated caustic. The zeros of both coordinates are placed in the waist of the caustic produced by an aberration-free reference sample. The BFS positions for the cases of the two lowest aberrations are placed on the z_0 axis. For larger aberrations, they can be found on the z axis. As shown in Fig. 2(a), every aberration of the optical system reduces the maximal intensity of the fundamental mode caustic, consistent with the Strehl ratio. However, Figs. 2(b)–2(d) show that the maximal intensity in the aberrated system exceeds those produced in diffraction-limited systems involving multimode-fiber sources for both positive and negative SAs. All aberration plots indicate that the maximal intensity curve is asymmetric with respect to the zero of z_0 coordinate. The ratio of the maximal intensity variation rate inside the ALR to that outside it depends on the source size. In our simulations, this ratio increased from 2 to 6 for the source size varying from 7 to 400 μm for the largest aberrations. This behavior of the calculated curves becomes clear upon considering the transverse LID shape dynamics, as shown in Fig. 3. For an aberration-free system, the transverse LID shapes may be considered symmetrical with respect to $z_0 = 0$ [Figs. 3(a) and 3(c)]. In the presence of an aberration, beam truncation occurs for the sequence indicated by the arrows 1 to 4. This yields formation of **M** and Π shapes inside the ALR. Outside ALR, the maximal intensity decreases much slower owing to the energy pumping from an approximately $1/e^2$ level into the peak (arrows 5). At the same time, the beam wings crawl off the axis, i.e., the full width at half maximum and $1/e^2$ beam sizes grow slower than the full size. It is important to note that in the presence of aberrations, the BFS cross section is always characterized by a Λ-shape LID, which is by no means the source's image [Figs. 3(b) and 3(d)]. These processes are common to both positive and negative aberrations, and the extent of their appearance depends solely on the relationship between the aberration strength and source size.

Our simulation results are consistent with classical analytic estimates[53,54] and agree with the results of other studies.[51,58,59,63] Yet, the defocusing ranges are considerably smaller than the ones reported by Pu and Zhang.[58] The claim that Gaussian beam focusing can be improved by introducing positive wave aberration[58] appears doubtful and requires reformulation. Simulation results by Park and Chung confirm this doubt.[59] Yet these authors have not reported submaximal axial intensity inside the ALR. Experimentally, a focused beam LID transformation has been reported by Kaplan,[51,63] but the author had not considered this finding. It is important to emphasize that an asymmetric caustic shape may cause considerable mistakes in Gaussian beam scaling for energetic estimates.

4 Experimental Results and Discussion

4.1 Experimental Setup and Methodology

Our experimental technique was based on conducting one parameter (WA$_{rms}$) at a time investigations. To this effect, two arrays (10, 11, 12, and 15, 16, 17) of identical transport systems with the same axial glass thickness, focal length, and NA were built. The numbering indicates our experimental schedule. The only difference between the systems within a given array was the value of the uncorrected wave SAs. This value was varied from 0.06 to 0.40 waves rms in BFS by altering the orientation and airspacing of the optical components. In this study, WA$_{rms}$ values were computed for each optical configuration by using standard optical design software. For the systems with smaller WA$_{rms}$ magnitudes, an additional experimental verification of the computed data was performed. For this, complete diffraction-limited reference analogs were assembled for the systems 10 and 15 using a different set of optical components. The Strehl ratio (S) was calculated as the ratio of the maximal waist intensity produced by the model system to the maximal
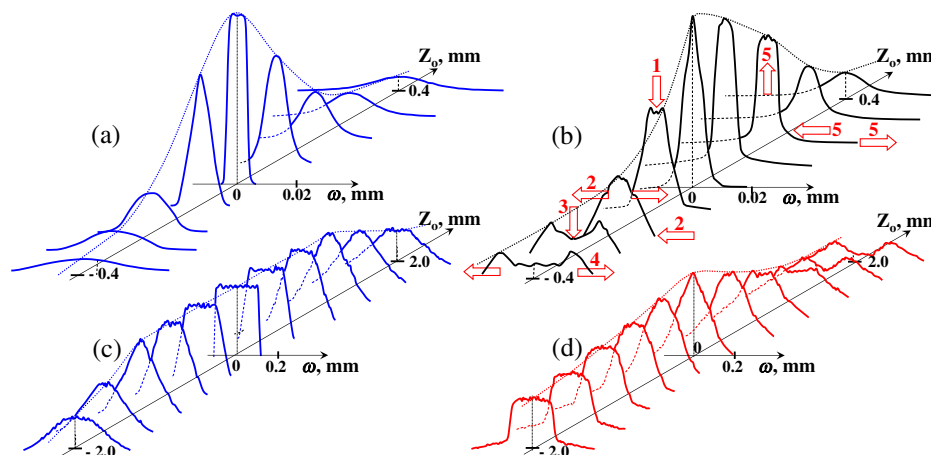

Fig. 3 Computed rotationally symmetric laser intensity distribution (LID) trains for: (a) Gaussian source $2\omega_S = 7$ μm, negligible SA, (b) the same source in the presence of 0.08λ WA$_{rms}$ positive wave SA, (c) uniform source $2\omega_S = 200$ μm, negligible SA, (d) the same source in the presence of 0.8λ WA$_{rms}$ negative wave SA. Object space NA is 0.10 and linear magnification is -1.175 for all figures.

waist intensity produced by its diffraction-limited correlate. The resulting S value was used to determine the WA_{rms} magnitude according to the famous approximated estimate $WA_{rms} \approx (2\pi)^{-1}\sqrt{1-S}$.[54] The computed and measured WA_{rms} magnitudes deviated by 6% and 14% from those of transport systems with WA_{rms} 0.06 and 0.08λ (experiments 10 and 15). For larger aberrations, the above estimate yields incorrect results.[54,70] All components of the transport systems were made of Heraeus Suprasil 3002 and Schott N-BK7HT with bulk absorption of 0.25 ppm $\times$ cm^{-1} and 2×10^{-4} cm^{-1}, respectively. We used commercial single-mode fiber lasers LC-0.4 and YLR-150/1500-QCW (International Photonics Group) with maximal continue wave powers of 400 and 250 W and output NA of about 0.05 ($2\omega_s = 14$ μm, $M^2 = 1.17$ and 1.05, respectively). In the systems 10–12 with linear magnification -1.70, aberrations were inserted at the collimation stage. In the systems 15–17 with linear magnification -1.05, aberrations were inserted at the focusing stage. The details of the transport systems can be found in our previous paper.[81] Wave SAs produced by these systems were positive.

A schematic of the experimental setup is shown in Fig. 4. The monitoring unit was rigidly attached to the cutting head and employed the same optics that were used for the cutting head assembly. The collimated laser beam was split to target the monitoring unit using a system of high-optical-quality wedges. The first of the wedges was periodically inserted into the beam path to allow for quasi-online monitoring. Our estimate of a thermally induced aberration (TIA) effect by combining the heating and probe beams have yielded TIA coefficients as small as 0.5×10^{-6} λ/W and 1×10^{-5} λ/W per 1 cm thickness for Suprasil 3002 and N-BK7HT, respectively. The TIA on the wedge-reflective surface was smaller than the detection threshold of our apparatus because the expansion coefficient was more than 20 times smaller than $\partial n/\partial T$.[55,72] In these conditions, the maximal TIA magnitudes were smaller than 10^{-3} waves for the systems 11 and 12 made of Suprasil 3002 with a 21 mm total axial thickness at 400 W laser power. The systems 10, 15, 16, and 17 that yielded the combination of 14 mm N-BK7HT and 11 mm

Fig. 4 Schematic diagram of the experimental setup.

Suprasil 3002 demonstrated about 10^{-2} waves total TIA strength. This allowed considering our trials free of thermally induced phenomena. The difference in optical paths in the working and monitoring arms was about 300 mm and did not affect any caustic shape alterations. The principal experimental complexity was associated with arranging the non-protected charge-coupled device surface coplanar with the upper surface of the cut sheet. This was achieved by registering the shadow pattern from the sliding beam of the He–Ne laser. The maintenance error was about ± 0.20 mm and was mostly caused by the sheet nonflatness. This error was considerably smaller than the length of an LID shape variation even for strongly aberrated beams.

4.2 Measured Profiles of a Cutting Beam

Figure 5 shows the LID shape trains registered in the monitoring channel for all transport systems and various axial coordinates. Apart from the difference caused by the varying NA values, the LID patterns for low-aberration systems 10 and 15 were qualitatively similar; thus, the LID train for the latter was omitted. The beam-waist size for the listed systems varied from 16 to 25 μm for systems 15 and 10 to 41–43 μm for systems 12 and 17. Regarding the differing aberration degradation of an initially Gaussian input beam, a Rayleigh range in its formal sense did not exceed 0.5 mm for each of the mentioned waist sizes. In the figure, this is marked in yellow and is included solely to indicate its correlation with the FPP range. The areas marked in blue and pink represent the FPP range, for which an excellent or acceptable cut quality was observed, respectively.

4.3 Experiments with Laser Cutting using Aberrated Beams

Low-pressure oxygen-assisted laser cutting experiments with the beams produced by the aforementioned optical systems were exactly conducted under the same conditions. The cut material was mild steel (C 0.14–0.22, Mn 0.3–0.6, Si < 0.05, P < 0.04, S < 0.05, Cr, Ni, Cu <0.3 mass % each). The assist gas was oxygen of 99.5% purity with 2.0–Bar pressure. We used the standard 1.0-mm Trumpf and Lasag nozzles with a 1.0-mm standoff distance. Material thickness was varied from 1 to 4 mm in 0.5-mm steps. The only parameter violating the one parameter at a time condition was a gradual decrease of the cutting speed with increasing sheet thickness. The cut speed was 5 to 30 mm/s and was kept constant for each thickness of the sheet. The cutting quality was estimated according to the minimal dross height. The cuts having dross height under 10 μm were qualified as excellent. Those with a dross height ranging from 10 to 200 μm were qualified as acceptable. Cuts having a dross height above 200 μm were classified as laser cutting failures. The minimal cut width was registered in FPP ranges termed "best cut FPP" and was as small as 0.3 mm for the maximal cut-sheet thickness. In the ranges termed "acceptable cut FPP," the cut widths were increased by up to 0.5 to 0.7 mm for the thickest sheets. The cut geometry was a 50-mm-long line, and the piercing point was outside the analysis range. Our experimental results are shown in Fig. 6, classified according to the above criteria. The FPP ranges yielding excellent cuts are highlighted in blue, and those yielding acceptable cuts are highlighted in pink. The
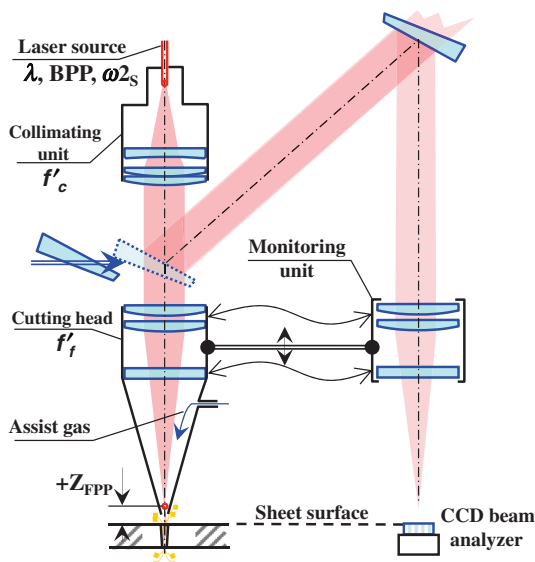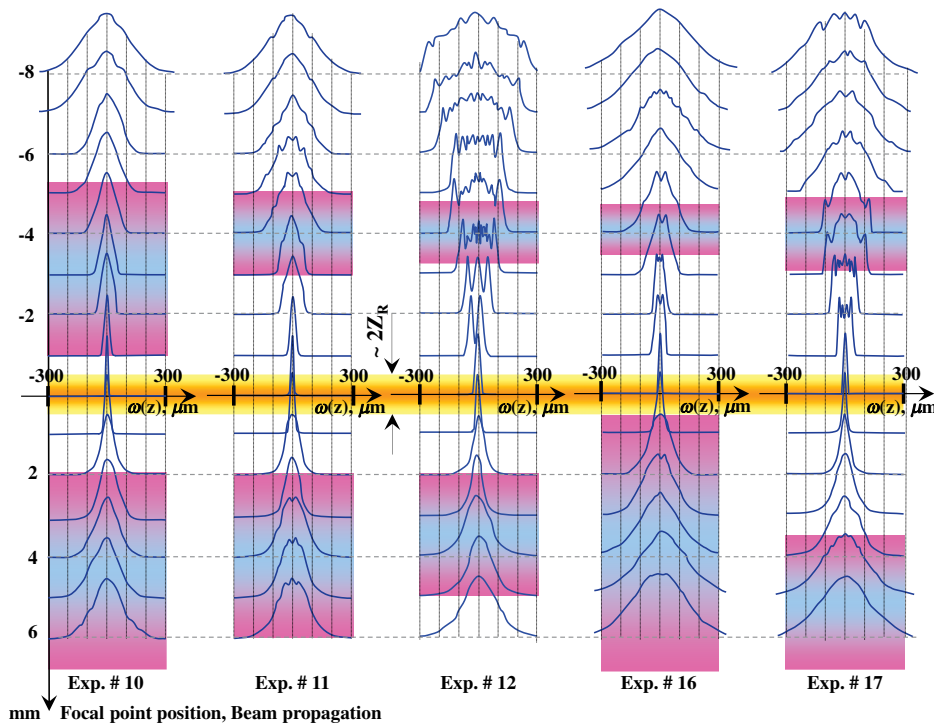
Fig. 5 Cross sections of rotationally symmetric transverse LIDs registered for the array of experimental optical systems. Marked regions show the FPP ranges where excellent and acceptable cuts have been obtained (see also Fig. 6). Each LID shape is normalized by its maximal amplitude.

rms strengths of the positive wave SAs, measured in units of waves, are given at the bottom of each diagram.

As in every laser cutting experiment, our data contain an unmistakable degree of noise. Nevertheless, a thorough inspection of the experimental results reveals the following: for each studied LID, it is possible to find a pair of positive

Fig. 6 The ranges of excellent (blue) and acceptable (pink) cut quality versus focal point position and material thickness. The experiment number is shown in the right upper corner of each diagram. The thermally induced aberration (TIA) contribution is not shown.

and negative ranges of the best cut FPP that produces an excellent laser-cut quality. In a similar manner, the cut quality qualifying as acceptable is allowed within a pair of considerably wider ranges of the FPP. Both positive ranges are considerably wider than the negative ones. The LID profile itself does not noticeably influence the cutting quality if the FPP is adjusted in the best cut and acceptable cut ranges. The width of the ranges is inversely proportional to the extent of SA. These facts may be consistently explained by employing the following model. Because no method has been developed for reliably predicting the focal point position, the best cut FPP is intuitively chosen from the highlighted region. This empirically provides the best thermal and hydrodynamic balance in the melt pool. In the space between a pair of acceptable cut FPPs, a too high laser intensity yields strong thermo- and hydrodynamic instabilities. The cutting quality becomes poor and only high-speed material separation is possible. Outside this space, the cutting process gradually moves from low-speed separation to the lack of throughout cut due to low laser intensities.

Under the constant performance of the laser source and a constant NA, the melt flow destabilization may be caused only by beam intensity variations. As seen from Fig. 5 in the region of positive FPP, the LID shape variation is insignificant so that the intensity variation is mostly caused by changing the divergent beam size. In contrast, for a negative FPP, the melt pool interacts with the part of the convergent beam with a rate of maximum intensity variation several times greater. Furthermore, a high maximum intensity variation is combined with a deep transverse modulation of the LID shape. The sum of these two properties makes the system much more sensitive to focal point position fluctuations and narrows the FPP range. We could not find any reliable
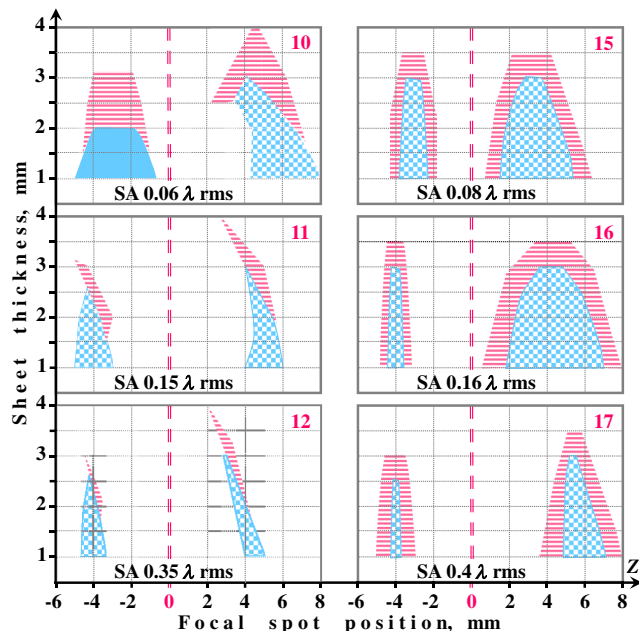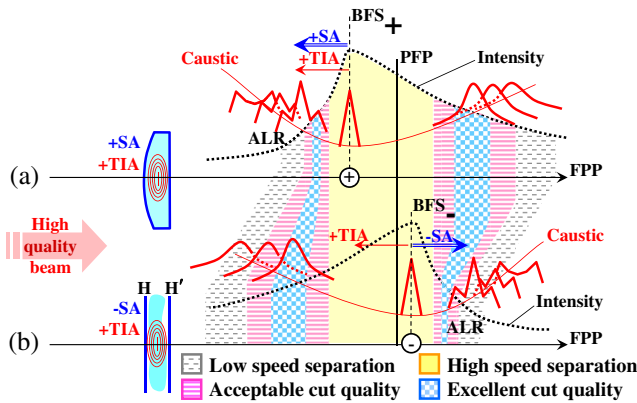
Fig. 7 Schematic of gas-assisted laser cutting with aberrated beams. (a) Thin red line shows the beam size measured at the $1/e^2$ level, dotted line shows the maximal intensity. (b) The scales for all plots are free.

difference in the cutting quality provided by the transport systems 10 and 15. This suggests that the crucial magnitude of the wave SA that worsens the cutting quality was about 0.1λ rms in our trials (here we have taken into account the 0.01λ contribution of TIA in the transport system 15). Taking into account the scattering of experimental data cited in Sec. 2, this implies that the given estimate may be characterized by other values under different experimental conditions. Most importantly, it can be caused by using small V-factor fiber lasers with complex and temporally unstable near-field LID shapes.

5 Conclusions

The performance of a laser cutting system is determined not only by the speed-power-pressure concept, but also by the focused beam spatial characteristics. In this paper, we demonstrate that a wave SA of few tenths of wavelength is sufficient for considerably altering the beam characteristics, and elucidate how an aberrational beam distortion effects on laser cutting quality. All aberrated beams produce a strongly asymmetric caustic shape. This offers no possibility of using Gaussian beam propagation for energy estimates of cutting performance and links the laser-melt pool interaction mode to an actual laser intensity distribution on the kerf front. A caustic asymmetry significantly contributes to asymmetrization of both the layout of FPPs pair relative to the BFS and to the possible range of FPP variation.

The particularity of the optical design of transport systems for powerful laser cutters suggests using dominantly positive lenses and optical materials with positive $\partial n/\partial T$. It leads to the situation in which the design and manufacturing SA as well as TIA amplify each other and cause an appreciable beam distortion, especially in the cases of low-M^2 lasers. This first results in the BFS moving toward the transport system. An ALR is always characterized by a truncated beam shape with strong transverse modulation; likewise, by strong axial variation of maximal intensity, as schematically shown in Fig. 7(a). This narrows the range of negative FPPs considerably, making the system much more sensitive to deviations from the best position. In contrast, a smooth appearance of a beam variation outside ALR significantly extends the range of the positive FPPs.

Negative wave SAs are unlikely in typical transport systems of gas-assisted cutters. Yet, they can appear in the case of a marked number of negative lenses. Examples of such systems are telephoto and reversed telephoto objectives focusing the radiation of solid-state and gas lasers and integrated finite optical systems for fiber lasers as well as F-Theta lenses for remote cutting machines. Our results show that in this case the character of the process is inversely changed, as shown in Fig. 7(b). The only difference is that the BFS position and caustic shape are caused by the competition of SA and TIA of opposite signs. Rigorous experimental verification of preliminary results for negative wave SAs' effect on cutting quality will be the direction for future work.

References

1. J. F. Ready, *Effects of High-Power Laser Radiation*, Academic Press, New York, London (1971).
2. The BOC Group, "Laser cutting. LASERLINE® Technical," (2015)
3. J. Powell, *The LIA Guide to Laser Cutting*, Laser Institute of America, ISBN 0-912035-17X (1999).
4. M. Brandt and S. Sun, "Laser-assisted machining: current status and future scope," in *Laser-Assisted Fabrication of Materials*, J. D. Majumdar and I. Manna, Eds., pp. 113–158, Springer-Verlag, Berlin and Heidelberg GmbH & Co. KG, Berlin (2012).
5. S. Sun and M. Brandt, "Laser beam machining," in *Nontraditional Machining Processes*, J. P. Davim, Ed., pp. 35–96, Springer-Verlag, London, New York (2013).
6. K. Kellens et al., "Energy and resource efficiency of laser cutting process," *Phys. Procedia* **56**, 854–864 (2014).
7. P. Hilton, "Parameter tolerance evaluation when laser cutting in decommissioning applications," in *Proc. 32nd Int. Cong. on Applications of Lasers and Electro-Optics (ICALEO 2013)*, Miami, Laser Institute of America, Orlando, Florida (2013).
8. J. K. Pocorni et al., "Measuring the state-of-the-art in laser cut quality," in *Proc. 14th Nordic Laser Materials Processing Conf. (NOLAMP 14)*, pp. 101–108, (2013).
9. M. Madic and M. Radovanovic, "Comparative modeling of CO_2 laser cutting using multiple regression analysis and artificial neural network," *Int. J. Phys. Sci.* **7**(16), 2422–2430 (2012).
10. M. Radovanovic and M. Madic, "Experimental investigations of CO_2 laser cut quality: a review," *Nonconv. Tech. Rev.* **4**, 35–42 (2011).
11. M. Hashemzadeh et al., "The application of specific point energy analysis to laser cutting with 1 μm laser radiation," *Phys. Procedia* **56**, 909–918 (2014).
12. A. M. Orishich et al., "Experimental comparison of laser cutting of steel with fiber and CO_2 lasers on basis of minimal roughness," *Phys. Procedia* **56**, 875–884 (2014).
13. S. O. Al-Mashikhi et al., "An explanation of 'striation free' cutting of mild steel by fibre laser," in *Proc. 5th Int. WLT-Conf. on Lasers in Manufacturing*, Munich, Germany, A. Ostendorf, T. Graf, and D. Petring, Eds., AT-Fachverlag GmbH, Stuttgart (2009).
14. S. R. Rajpurohit and D. M. Patel, "Striation mechanism in laser cutting–the review," *Int. J. Eng. Res. Appl.* **2**(2), 457–461 (2012).
15. K. Hirano and R. Fabbro, "Possible explanations for different surface quality in laser cutting with 1 micron and 10 microns beams," *J. Laser Appl.* **24**(1), 012006 (2012).
16. K. Hirano and R. Fabbro, "Experimental investigation of hydrodynamics of melt layer during laser cutting of steel," *J. Phys. D: Appl. Phys.* **44**(10), 105502 (2011).
17. B. D. Prajapati, R. J. Patel, and B. C. Khatri, "Parametric investigation of CO_2 laser cutting of mild steel and Hardox-400 material," *Int. J. Emerg. Technol. Adv. Eng.* **3**(4), 204–208 (2013).
18. P. S. Chaudhari and D. M. Patel, "Parametric effect of fiber laser cutting on surface roughness in 5 mm thick mild steel sheet (IS-2062)," *Int. J. Eng. Res. Technol.* **1**(6), 1–6 (2012).
19. M. Zaied et al., "Effect of laser cutting parameters on surface quality of low carbon steel (S235)," *J. Achiev. Mater. Manuf. Eng.* **54**(1), 128–134 (2012).
20. M. Sowjanya and G. Y. Gowd, "Empirical modeling and analysis of laser beam cutting process," *Int. J. Innovative Tech. Res.* **1**(5), 411–416 (2013).
21. Sivarao et al., "RSM based modeling for surface roughness prediction in laser machining," *Int. J. Eng. Tech. IJTT-IJENS.* **10**(4), 32–39 (2010).
22. R. Phipon and B. B. Pradham, "Control parameters optimization of laser beam machining using genetic algorithm," *Int. J. Comp. Eng. Res.* **2**(5), 1510–1516 (2012).
23. Sivaraos et al., "Comparison between Taguchi method and response surface methodology (RSM) in modelling CO_2 laser machining," *Jordan J. Mech. Ind. Eng* **55**(8), 35–42 (2014).

24. M. L. Cadorette and H. F. Walker, "Characterizing productivity of a 4kw CO_2 laser cutting system for 0.25" mild steel using central composite methodology," *J. Ind. Technol.* **22**(2), 1–8 (2006).
25. B. S. Yilbas, "Laser cutting quality assessment and thermal efficiency analysis," *J. Mater. Proc. Tech.* **155–156**, 2106–2115 (2004).
26. B. J. Ranaganth and G. Viswanath, "Application of artificial neural network for optimizing cutting variables in laser cutting of 304 grade stainless steel," *Int. J. Appl. Eng. Tech.* **1**(1), 106–112 (2011).
27. A. K. Pandey and A. K. Dubey, "Intelligent modeling of laser cutting of thin sheet," *Int. J. Model. Optim.* **1**(2), 107–112 (2011).
28. M. Madic, M. Radovanovic, and M. Gostimirovic, "ANN modeling of kerf taper angle in CO_2 laser cutting and optimization of cutting parameters using Monte Carlo method," *Int. J. Ind. Eng. Comp.* **6**(1), 33–42 (2015).
29. M. Manohar, "CO2 laser beam cutting of steels: Material issues," *J. Laser Appl.* **18**(2), 101–112 (2006).
30. V. G. Niziev and A. V. Nesterov, "Influence of beam polarization on laser cutting efficiency," *J. Phys. D: Appl. Phys.* **32**, 1455–1461 (1999).
31. R. Weber et al., "Effects of radial and tangential polarization in laser material processing," *Phys. Procedia* **12**, 21–30 (2011).
32. L. D. Scintilla et al., "A comparative study of cut front profiles and absorptivity behavior for disk and CO2 laser beam inert gas fusion cutting," *J. Laser Appl.* **24**(5), 052006 (2012).
33. F. Ullman et al., "Highspeed laser ablation cutting of metal," *Proc. SPIE* **8603**, 860311 (2013).
34. M. Essien and P. W. Fuerschbach, "Beam characterization of a material processing CO2 laser," *Weld. Res. Suppl.* 47s–54s (1996).
35. C. Wandera, "Laser cutting of austenitic stainless steel with a high quality laser beam," MS Thesis, Lappeenranta (2006).
36. C. Wandera, "Performance of high power fibre laser cutting of thick-section steel and medium-section aluminium," Thesis for the degree of Doctor of Science, Lappeenranta Univ. of Technology (2010).
37. M. Kristiansen et al., "Quality and performance of laser cutting with a high power SM fiber laser," in *Proc. 14th Nordic Laser Materials Processing Conf. (NOLAMP 14)*, A. Kaplan and Hans Engstrom, Eds., pp. 109–120, Gothenburg, Sweden (2013).
38. J. E. S. Petersen and H. D. Jensen, "High quality laser cutting in aluminium," MS Thesis, Aalborg University (2012).
39. H. Kogelnik and T. Li, "Laser beams and resonators," *Appl. Opt.* **5**(10), 1550–1567 (1966).
40. S. Safdar, L. Li, and M. A. Sheikh, "Numerical analysis of the effects of non-conventional laser beam geometries during laser melting of metallic materials," *J. Phys. D: Appl. Phys.* **40**, 593–603 (2007).
41. H. Ozaki et al., "Cutting properties of austenitic stainless steel by using laser cutting process without assist gas," in *Advances in Optical Tech.*, Hindawi Publishing Corp., Vol. **2012**, article ID 234321, (2012).
42. Y. Li et al., "Lumped parameter model for multimode laser cutting," *Opt. Lasers Eng.* **35**, 371–386 (2001).
43. F. O. Olsen, "Laser metal cutting with tailored beam pattern," *Ind. Laser Solutions.* **26**(5), 17–19 (2011).
44. C. Caristan and J. Finn, "Fiber laser blanking of coil strips at extreme speed–extreme power," in *Proc. 28th Int. Cong. on Applications of Lasers and Electro-Optics (ICALEO 2009)*, Orlando, Laser Institute of America, Orlando, Florida (2009).
45. M. R. Kronthaler, S. Braunreuther, and M. F. Zaeh, "Bifocal hybrid laser welding – more than a superposition of two processes," *Phys. Procedia* **12**, 208–214 (2011).
46. B. J. Zhan and M. J. Yang, "Influences of laser spot on high-speed welding for Cr-plated sheets," *Weld. J.* **92**(10), 291s–296s (2013).
47. H. Schwede et al., "Multi spot laser beam processing. Fundamentals—Applications—Diagnostics—Quality Assessment," in *Proc. 20th Int. Cong. on Applications of Lasers and Electro-Optics (ICALEO 2001)*, Jacksonville, Laser Institute of America, Orlando, Florida (2001).
48. K. S. Hansen, M. Kristiansen, and F.O. Olsen, "Beam shaping to control of weldpool size in width and depth," *Phys. Procedia* **56**, 467–476 (2014).
49. B. Victor et al., "Custom beam shaping for high-power fiber laser welding," *Weld. J.* **90**(6), 113s–120s (2011).
50. J. Volpp, "Investigation on the influence of different laser beam intensity distributions on keyhole geometry during laser welding," *Phys. Procedia* **39**, 17–26 (2012).
51. A. F. H. Kaplan, "Modelling the primary impact of an Yb:fibre laser beam profile on the keyhole front," *Phys. Procedia* **12**, 627–637 (2011).
52. H. D. Doan, I. Naoki, and F. Kazuyoshi, "Laser processing by using fluidic laser beam shaper," *Int. J. Heat Mass Transfer* **64**, 263–268 (2013).
53. W. T. Welford, *Aberrations of Optical Systems*, Adam Hilger, Bristol, Philadelphia and New York (1986).
54. M. Born and E. Wolf, *Principles of Optics*, 7th ed., Cambridge University Press, Cambridge (1999).
55. C. A. Klein, "High-energy laser windows: case of fused silica," *Opt. Eng.* **49**(9), 091006 (2010).
56. C. A. Klein, "Optical distortion coefficients of high-power laser windows," *Opt. Eng.* **29**(4), 343–350 (1990).
57. P. Herwig and J. Hauptmann, "Aberrations induced by high brightness lasers," in *14th Nordic Laser Materials Processing Conf. (NOLAMP 14)*, pp. 359–367 (2013).
58. J. Pu and H. Zhang, "Intensity distribution of Gaussian beams focused by a lens with spherical aberration," *Opt. Commun.* **151**, 331–338 (1998).
59. S. J. Park and C. S. Chung, "Influence of Bessel and Bessel-Gauss beams on the point spread function and the encircled energy," *J. Korean Phys. Soc.* **30**(2), 194–201 (1997).
60. A. E. Siegman, "Defining, measuring, and optimizing laser beam quality," *Proc. SPIE* **1868**, 2–12 (1993).
61. T. M. Jeong and J. Lee, "Accurate determination of the beam quality factor of an aberrated high-power laser pulse," *J. Korean Phys. Soc.* **55**(2), 488–494 (2009).
62. C. Mafusire and A. Forbes, "Propagating aberrated light," *Proc. SPIE* **8236**, 82360E (2012).
63. A. F. H. Kaplan, "Analysis and modeling of a high-power Yb:fiber laser beam profile," *Opt. Eng.* **50**(5), 054201 (2011).
64. H. Schwede et al., "Characterizing high power laser beams to detect the thermal load of optics and to identify other limitations within the design of the optical system," *Proc. SPIE* **7193**, 71930E (2009).
65. "Lasers and laser-related equipment—Test methods for laser beam widths, divergence angles and beam propagation ratios," International standard ISO 11146 (2005).
66. T. Kaiser et al., "Complete modal decomposition for optical fibers using CGH-based correlation filters," *Opt. Express* **17**(11), 9347–9356 (2009).
67. O. A. Schmidt et al., "Real-time determination of laser beam quality by modal decomposition," *Opt, Express* **19**(7), 6741–6748 (2011).
68. H. S. Kim et al., "Numerical investigation of the beam characteristics of a combination of two coherent laser beams," *J. Korean Phys. Soc.* **59**(5), 3224–3228 (2011).
69. A. E. Siegman, "Laser beams and resonators: beyond the 1960s," *IEEE J. Sel. Top. Quantum Electron.* **6**(6), 1389–1399 (2000).
70. V. N. Mahajan, "Strehl ratio for primary aberrations: some analytical results for circular and annular pupils," *J. Opt. Soc. Am.* **72**, 1258–1266 (1982).
71. E. Perevezentsev, A. Poteomkin, and E. Khazanov, "Comparison of phase-aberrated laser beam quality criteria," *Appl. Opt.* **46**(5), 774–784 (2007).
72. R. Chou et al., "Thermally induced distortion of a high-average-power laser system by an optical transport system," *Proc. SPIE* **3782**, 246–254 (1999).
73. II-IV-HighYAG, "High Performance on Best Focus," Laser Processing Head BIMO, http://www.highyag.com/resources/pdf/laser-processing-BIMO.pdf (2015).
74. W. J. Smith, *Modern Lens Design*, 2nd ed., McGraw-Hill Companies, SPIE Press, New York etc., (2005).
75. M. Silva-Lopez, J. M. Rico-Garsia, and J. Alda, "Measurement limitations in knife-edge tomographic phase retrieval of focused IR laser beams," *Opt. Express* **20**(21), 23875–23866 (2012).
76. M. Blomqvist et al., "All-in-quartz optics for low focal shifts," *Proc. SPIE* **7912**, 791216 (2011).
77. O. Blomster et al., "Optics performance at high-power levels," *Proc. SPIE* **6871**, 68712B (2008).
78. J. F. Bisson and H. Sako, "Suppression of the focal shift of single-mode laser with a miniature laser processing head," *J. Laser Micro/Nanoeng.* **4**(3), 170–176 (2009).
79. J. D. Mansel et al., "Evaluating the effect of transmissive optic thermal lensing on laser beam quality with a Shack-Hartmann wave-front sensor," *Appl. Opt.* **40**(3), 366–374 (2001).
80. S. Ream et al., "Zinc sulfide optics for high power laser applications," in *Proc. 26th Int. Cong. on Applications of Lasers and Electro-Optics (ICALEO 2007)*, Orlando, Laser Institute of America, Orlando, Florida (2007).
81. V. Yurevich et al., "Aberration beam shaping in laser cutting with large aspect ratios," *Proc. SPIE* **8963**, 89630Y (2014).

Vladimir I. Yurevich received his PhD degree from the Institute for Fine Mechanics and Optics at St. Petersburg in 1989. He worked for the IFMO and for St. Petersburg University. He joined the Laser Center in 2000 as a head of the Laser and Optics Department. He also holds a position at ITMO National Research University. His research interests include lasers and beams, optical design, and laser–matter interaction. He has published 35 papers and holds 8 patents.

Sergey G. Gorny is the director of the Laser Center Ltd. He received his PhD degree from the Polytechnic Institute at St. Petersburg in 1986. He is the author of more than 130 papers. His current research interests include laser machining and laser–matter interaction. He also actively works for St. Petersburg State Polytechnical University.

Biographies of the other authors are not available.